Supplementary Information

Machine Learning-Assisted Ultrafast Flash Sintering of High-Performance and Flexible Silver-Selenide Thermoelectric Devices

Mortaza Saeidi-Javash,[a,c] Ke Wang,[b] Minxiang Zeng,[a,d] Tengfei Luo,[a,b] Alexander W. Dowling,[b] and Yanliang Zhang[a]*

[a] Department of Aerospace and Mechanical Engineering, University of Notre Dame, Notre Dame, IN 46556, USA

[b] Department of Chemical and Biomolecular Engineering, University of Notre Dame, Notre Dame, IN 46556, USA

[c] Department of Mechanical and Aerospace Engineering, California State University Long Beach, Long Beach, CA 90840, USA

[d] Department of Chemical Engineering, Texas Tech University, Lubbock, TX 79409, USA

*Corresponding Author: yzhang45@nd.edu

Content

Figure S1. Schematic demonstrating the synthesis of silver-selenide nanostructures and fabrication process on porous membrane.

Figure S2. Digital photos of silver-selenide films made by vacuum-assisted filtration technique **(a)** before, **(b)** after cold pressing at 25 MPa for 15 minutes. Scale bar is 1 cm. **(c)** Demonstrating the flexibility of the fabricated film before sintering.

Table S1. Details of intense pulsed light (flash) sintering conditions for each experiment.

Figure S3. Correlation between concentration of the silver-selenide solution and thickness of the fabricated films (solvent was 40 ml ethanol).

Figure S4. **(a)** XRD pattern of synthesized silver-selenide nanostructures. Surface SEM images at **(b)** low, and **(c)** high magnification of the fabricated film.

Figure S5. Cross-sectional SEM-EDX map of element distribution of unsintered silver-selenide on porous filtration membrane.

Table S2. EDX map of element distribution of unsintered silver-selenide film after fabrication.

Figure S6. Room temperature TE properties of unsintered and flash sintered silver-selenide TE films under non-optimum (experiment 24) and optimum (experiment 32) sintering variables (see details of sintering conditions for experiments 24, and 32 in **Table S1**). **(a)** The electrical conductivity, and the Seebeck coefficient. **(b)** Power factor.

Figure S7. XRD pattern of unsintered and sintered silver-selenide film under the optimum variables (experiment 32).

Table S3. Room temperate TE and carrier transport properties of unsintered and flash sintered silver-selenide films under the optimal condition.

Table S4. EDS map of element distribution of flash sintered silver-selenide film under the optimized condition (experiment 32).

Figure S8. Room temperature TE properties of flash sintered silver-selenide TE films with 2.3 μm and 14.3 μm thicknesses under the same input energy of ~2.54 J (experiments 6, and 28: 2.4 kV voltage, 2 ms pulse duration, and single pulse). **(a)** The electrical conductivity, and the Seebeck coefficient. **(b)** Power factor.

Figure S9. Optical microscopy image showing sublimation of the silver-selenide nanostructures under excessive input energy.

Figure S10. Impact of reducing pulse delay time on power factor of the flash sintered silver-selenide TE films under the same input energy (i.e., fixed voltage, pulse duration, and number of pulses).

Figure S11. Cross-sectional SEM images of the sintered film under the optimal variables (experiment 32).

Figure S12. Cross-sectional SEM image of the flash sintered film under the optimized condition (experiment 32) used for thermal diffusivity measurement. Scale bars in **(a)**, and **(b)** are 50 μm, and 2 μm, respectively.

Figure S13. Bayesian optimization prediction mean, uncertainty and expected improvement from all data except the highest power factor.

Figure S14. Feature-feature correlation matrix of the top features.

Figure S15. Flexibility test of the flash sintered films under different bending angels.

Table S5. Comparison for flexibility of silver-selenide films with different compositions fabricated using vacuum-assisted filtration technique

Figure S16. (a) Experimental setup for TEG performance measurement. **(b)** In-plane TEG assembled with six silver-selenide TE films on mica. Scale bar is 1 cm.

Figure S17. (a) Schematic illustration of the thermal diffusivity measurement setup, and **(b)** recorded temperatures.

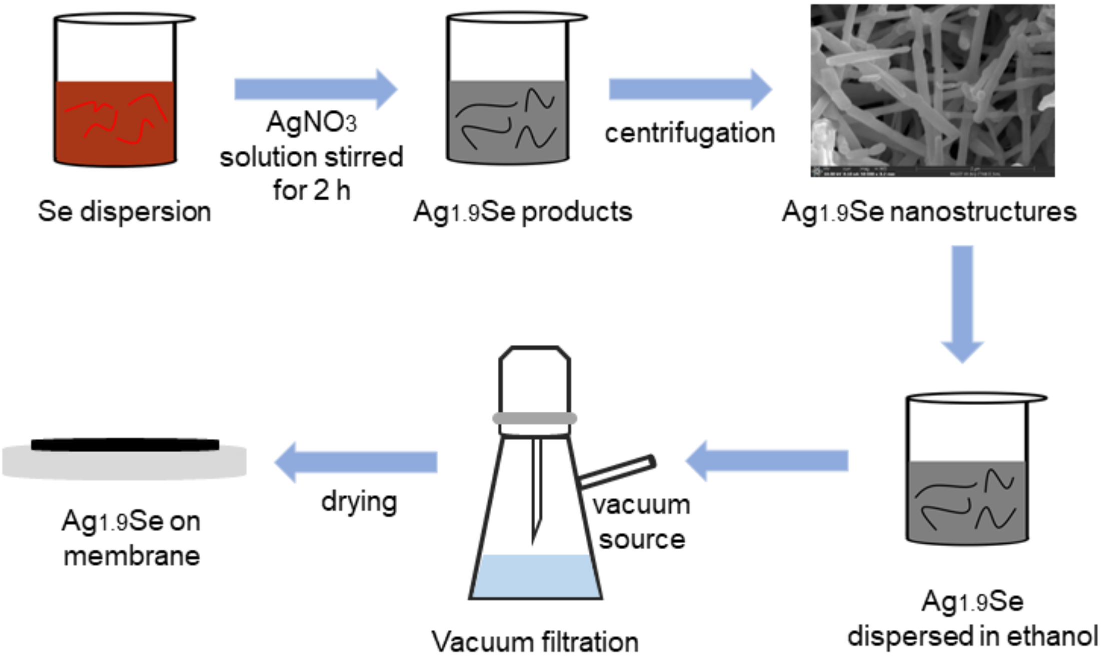

Figure S1. Schematic demonstrating the synthesis of silver-selenide nanostructures and fabrication process on porous membrane.

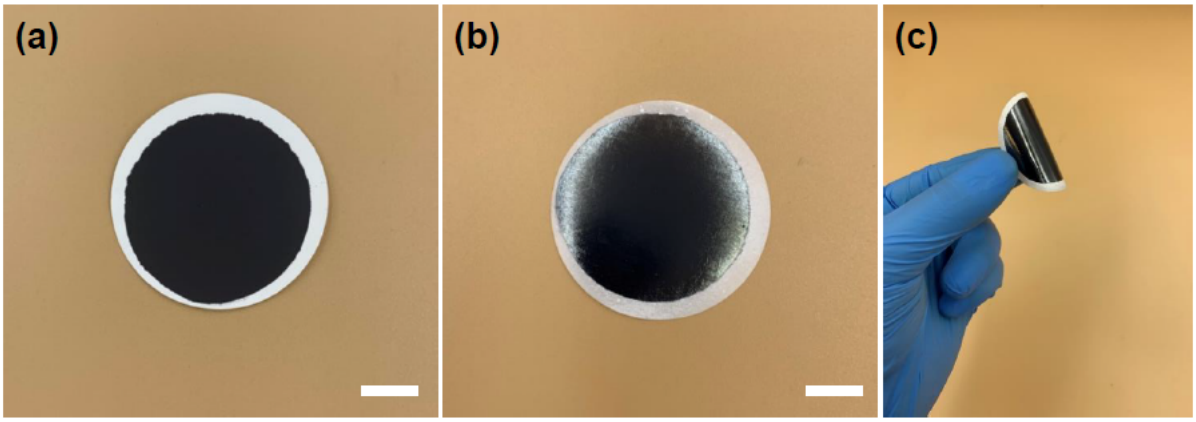

Figure S2. Digital photos of silver-selenide films made by vacuum-assisted filtration technique **(a)** before, **(b)** after cold pressing at 25 MPa for 15 minutes. Scale bar is 1 cm. **(c)** Demonstrating the flexibility of the fabricated film before sintering.

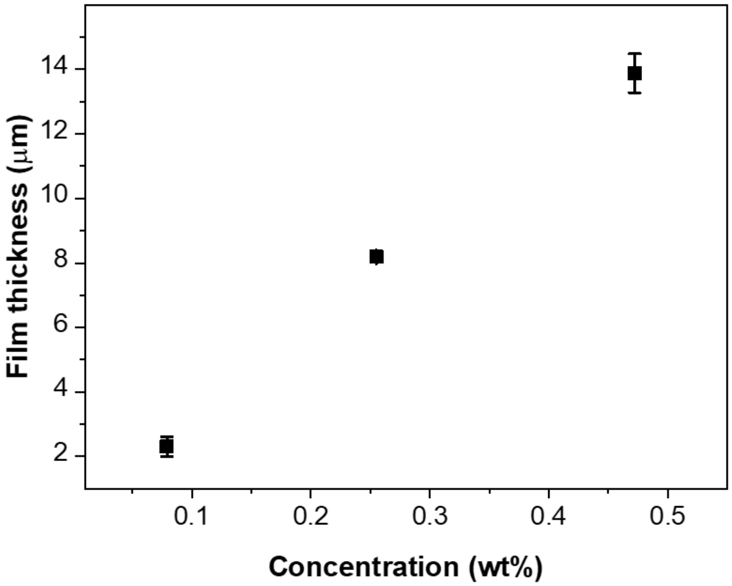

Figure S3. Correlation between concentration of the silver-selenide solution and thickness of the fabricated films. (solvent was 40 ml ethanol)

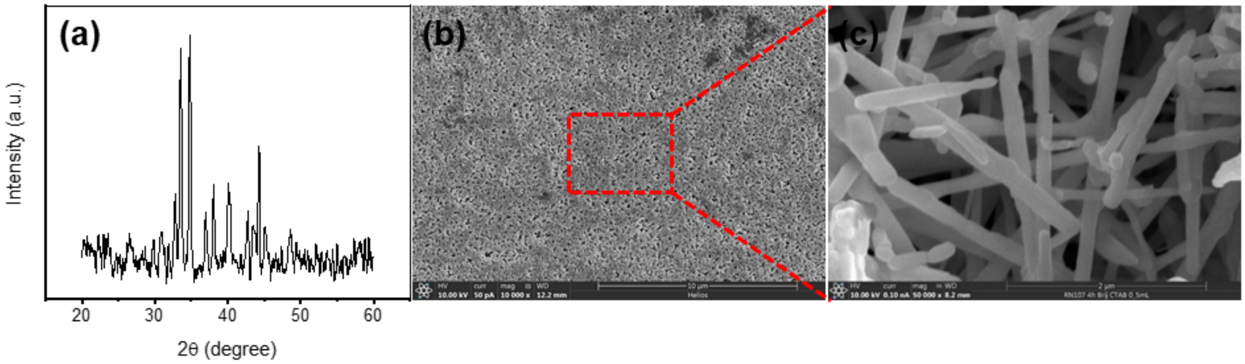

Figure S4. (a) XRD pattern of synthesized silver-selenide nanostructures. Surface SEM images at **(b)** low, and **(c)** high magnification of the fabricated film.

Table S1. Details of intense pulsed light (flash) sintering conditions for each experiment.

Experiment number	Thickness group (µm)	Thickness subgroup (µm)	Voltage (kV)	Power density (kW/cm²)	Pulse duration (ms)	Number of pulses	Pulse delay time (ms)	Total sintering time (ms)	Total deposited energy on TE film (J)
1	12.5 ± 3.2	14.3	2.2	3.47	1	1	0	1	1.04
2			2.2	3.47	2	1	0	2	2.08
3			2.4	4.24	1	1	0	1	1.27
4			2.2	3.47	1	5	1000	4005	5.20
5			2.4	4.24	1	5	1000	4005	6.35
6			2.4	4.24	2	1	0	2	2.54
7		16.5	2.4	4.24	2.5	1	0	2.5	3.18
8			2.2	3.47	2.5	1	0	2.5	2.60
9			2.6	5.09	2.1	1	0	2.1	3.21
10			2.6	5.09	2.5	1	0	2.5	3.82
11			2.8	6.04	2.1	1	0	2.1	3.80
--		13.3	2.8	6.04	2.3	1	0	2.3	4.17
--			2.9	6.54	2.1	1	0	2.1	4.12
--			2.9	6.54	2.3	1	0	2.3	4.52
12			2.7	5.55	0.9	4	1500	4503.6	6.00
13			2.7	5.55	0.9	10	1500	13509	14.99
14		9	2.7	5.55	0.9	4	248	747.6	6.00
15			2.7	5.55	0.9	10	248	2241	14.99
16			2.6	5.09	1.2	5	1000	4006	9.16
17			2.6	5.09	1.2	10	1000	9012	18.33
18			2.6	5.09	1.2	5	298	1198	9.16
19			2.6	5.09	2.1	2	490	494.2	6.41
20			2.6	5.09	2.1	2	1000	1004.2	6.41
21			2.6	5.09	1.7	2	404	407.4	5.19
22			2.6	5.09	1.7	4	404	1218.8	10.39
--	2.6 ± 0.5	2.3	2.8	6.04	1.5	8	420	2952	21.73
--			2.7	5.55	1.7	10	440	3977	28.32
--			2.65	5.32	1.8	11	450	4519.8	31.60
--			2.6	5.09	1.9	12	460	5082.8	34.82
--			2.55	4.87	2	13	470	5666	37.98
23			2.2	3.47	0.5	1	0	0.5	0.52
24			2.2	3.47	1	1	0	1	1.04
25			2.2	3.47	2	1	0	2	2.08
26			2.4	4.24	0.5	1	0	0.5	0.64
27			2.4	4.24	1	1	0	1	1.27
28			2.4	4.24	2	1	0	2	2.54
29			2.1	3.12	2	2	340	344	3.74
30			2.15	3.29	1.9	2	340	343.8	3.75

31		2.4	2.2	3.47	1.5	4	270	816	6.24
32			2.3	3.84	1.5	4	293	885	6.91
33		2.7	2.3	3.84	1.6	6	314	1579.6	11.06
34			2.2	3.47	2.2	2	413	417.4	4.58
35			2.3	3.84	1.7	10	335	3032	19.58
36		3.8	2.35	4.03	1.5	2	310	313	3.63
37			2.2	3.47	1.5	7	270	1630.5	10.92

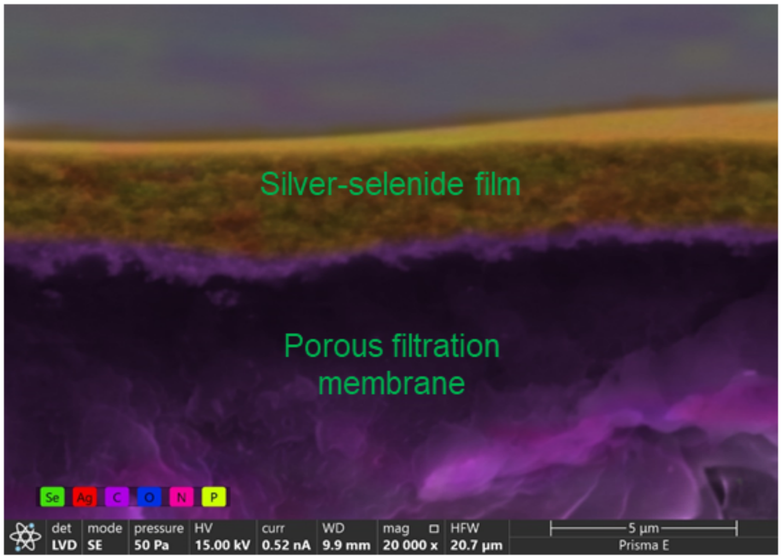

Figure S5. Cross-sectional SEM-EDS map of element distribution of unsintered silver-selenide on porous filtration membrane.

Table S2. EDS map of element distribution of unsintered silver-selenide film after fabrication.

Element	Atomic %	Atomic % Error	Weight %	Weight % Error
C	44.0	0.1	12.7	0.0
N	2.6	0.1	0.9	0.0
O	19.4	0.1	7.6	0.0
Se	11.7	0.0	22.2	0.1
Ag	22.3	0.0	56.4	0.0

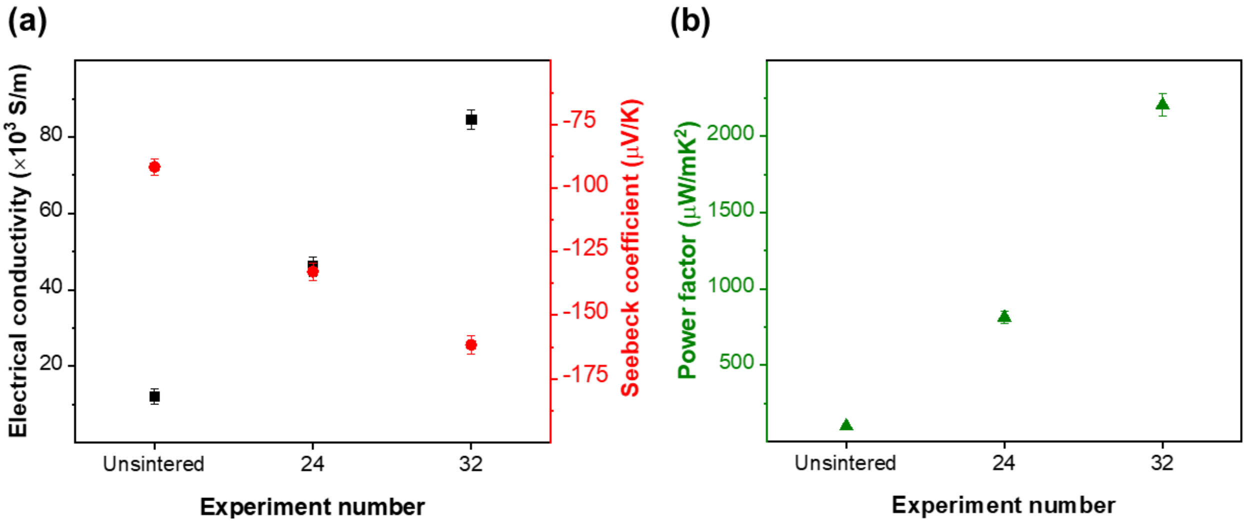

Figure S6. Room temperature TE properties of unsintered and flash sintered silver-selenide TE films under non-optimum (experiment 24) and optimum (experiment 32) sintering variables (see details of sintering conditions for experiments 24, and 32 in **Table S1**). **(a)** The electrical conductivity, and the Seebeck coefficient. **(b)** Power factor.

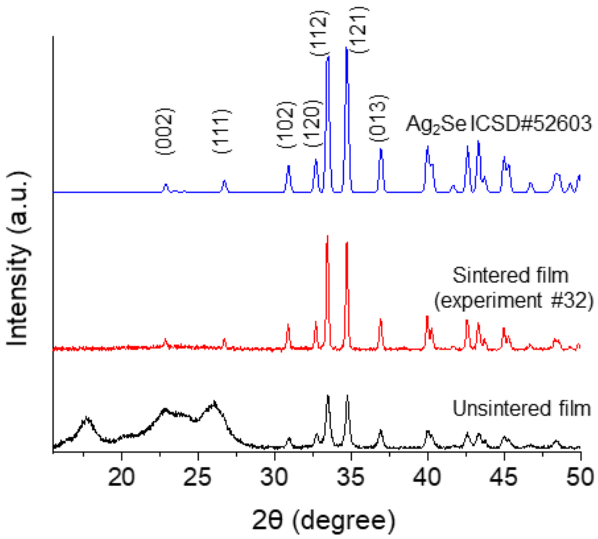

Figure S7. XRD pattern of unsintered and sintered silver-selenide film under the optimum variables (experiment 32).

Table S3. Room temperate TE and charge carrier transport properties of unsintered and flash sintered silver-selenide films under the optimal condition.

Sintering condition	Input energy (J)	σ (10^4 S/m)	S (μV/K)	PF (μW/mK^2)	n (10^{19} cm^{-3})	μ (cm^2 V^{-1} s^{-1})
Unsintered	0.0	1.18	-90.6	97.2	1.14	64.9
Optimal sintering (experiment 32)	6.9	8.47	-160.2	2174.4	0.73	721.3

Table S4. EDS map of element distribution of flash sintered silver-selenide film under the optimal sintering condition (experiment 32).

Element	Atomic %	Atomic % Error	Weight %	Weight % Error
C	22.7	0.2	4.2	0.0
O	11.2	0.3	2.7	0.1
N	2.4	0.1	2.2	0.1
Se	20.3	0.1	24.6	0.1
Ag	39.9	0.0	65.6	0.0

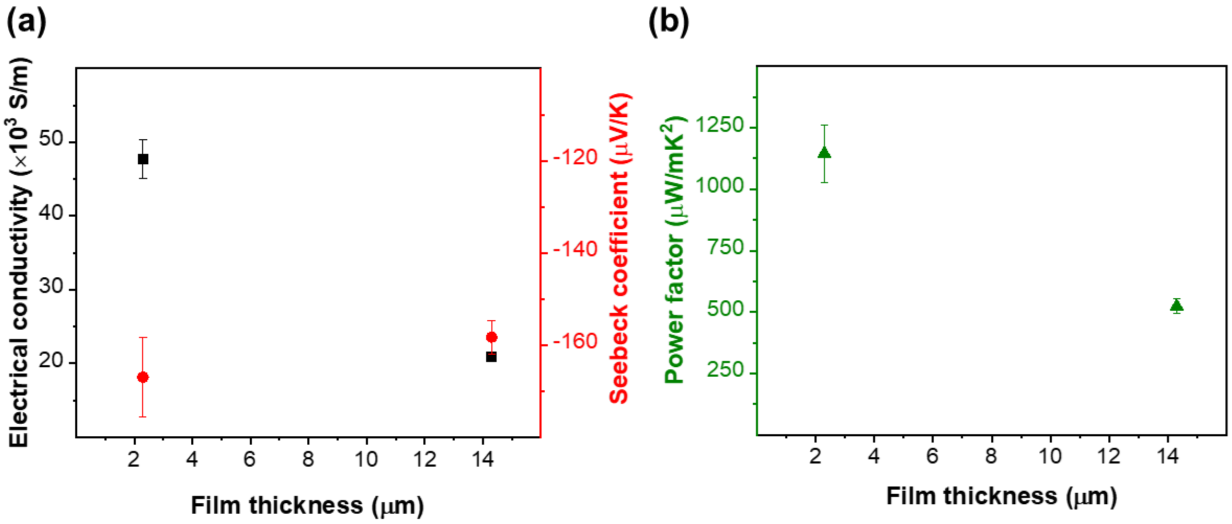

Figure S8. Room temperature TE properties of flash sintered silver-selenide TE films with 2.3 μm and 14.3 μm thicknesses under the same input energy of ~2.54 J (experiments 6, and 28: 2.4 kV voltage, 2 ms pulse duration, and a single pulse). **(a)** The electrical conductivity, and the Seebeck coefficient. **(b)** Power factor.

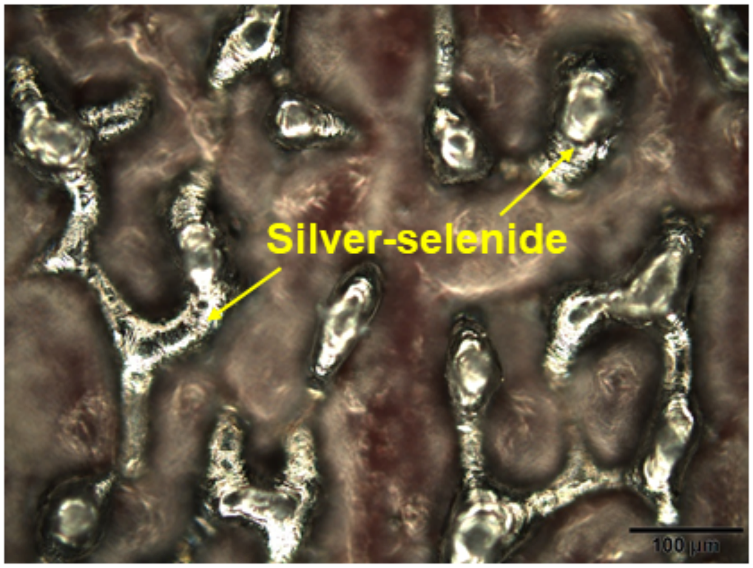

Figure S9. Optical microscopy image showing sublimation of the silver-selenide nanostructures under excessive input energy.

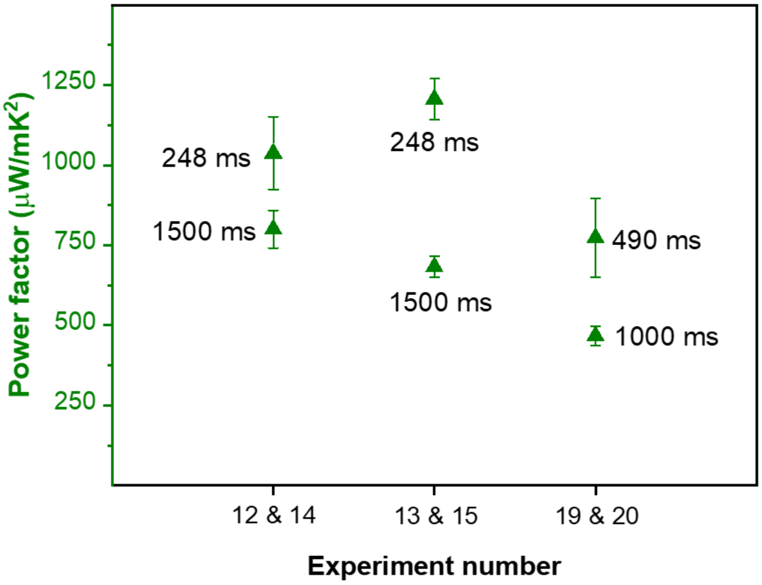

Figure S10. Impact of reducing pulse delay time on PF of the flash sintered silver-selenide TE films under the same input energy (i.e., fixed voltage, pulse duration, and number of pulses).

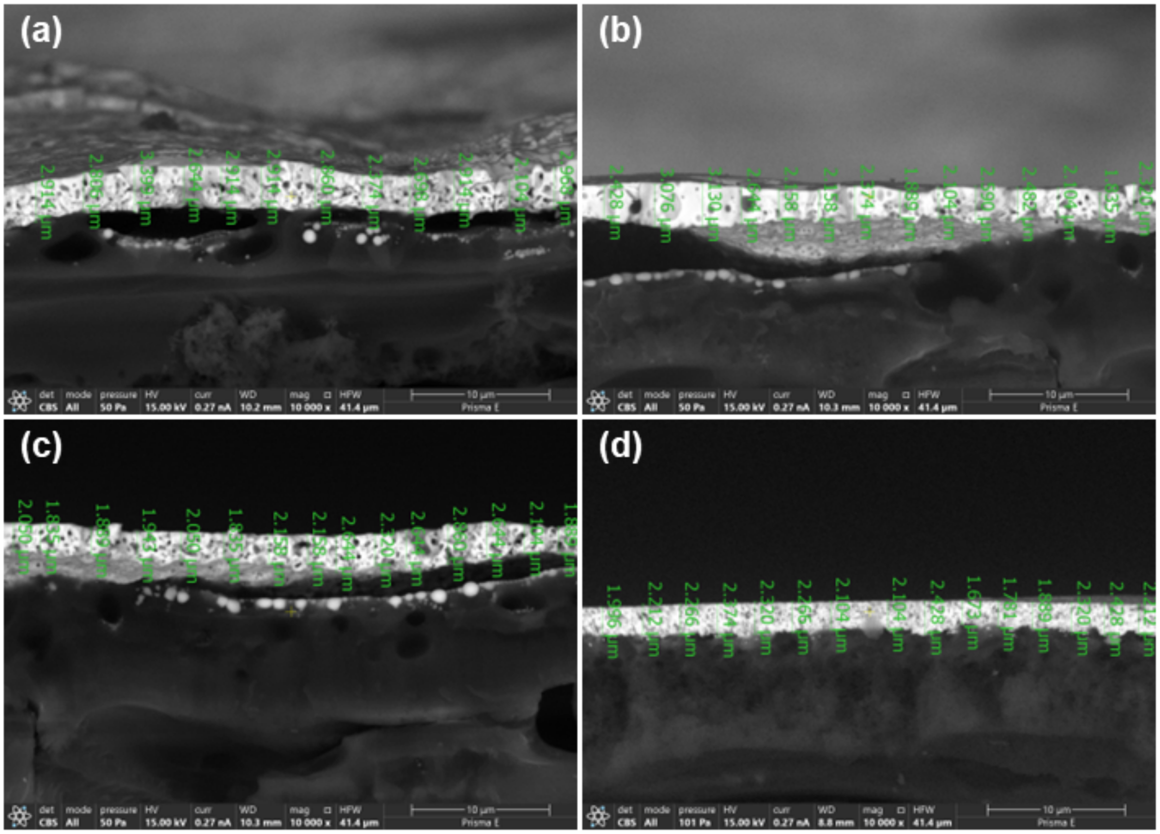

Figure S11. Cross-sectional SEM images of the sintered film under the optimal condition (experiment 32).

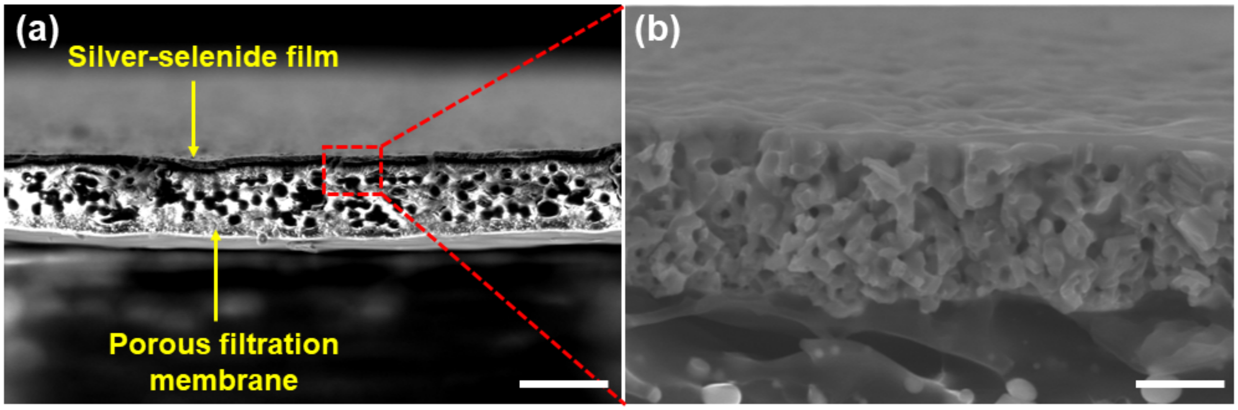

Figure S12. Cross-sectional SEM image of the flash sintered film under the optimized condition (experiment 32) used for thermal diffusivity measurement. Scale bars in **(a)** and **(b)** are 50 µm, and 2 µm, respectively.

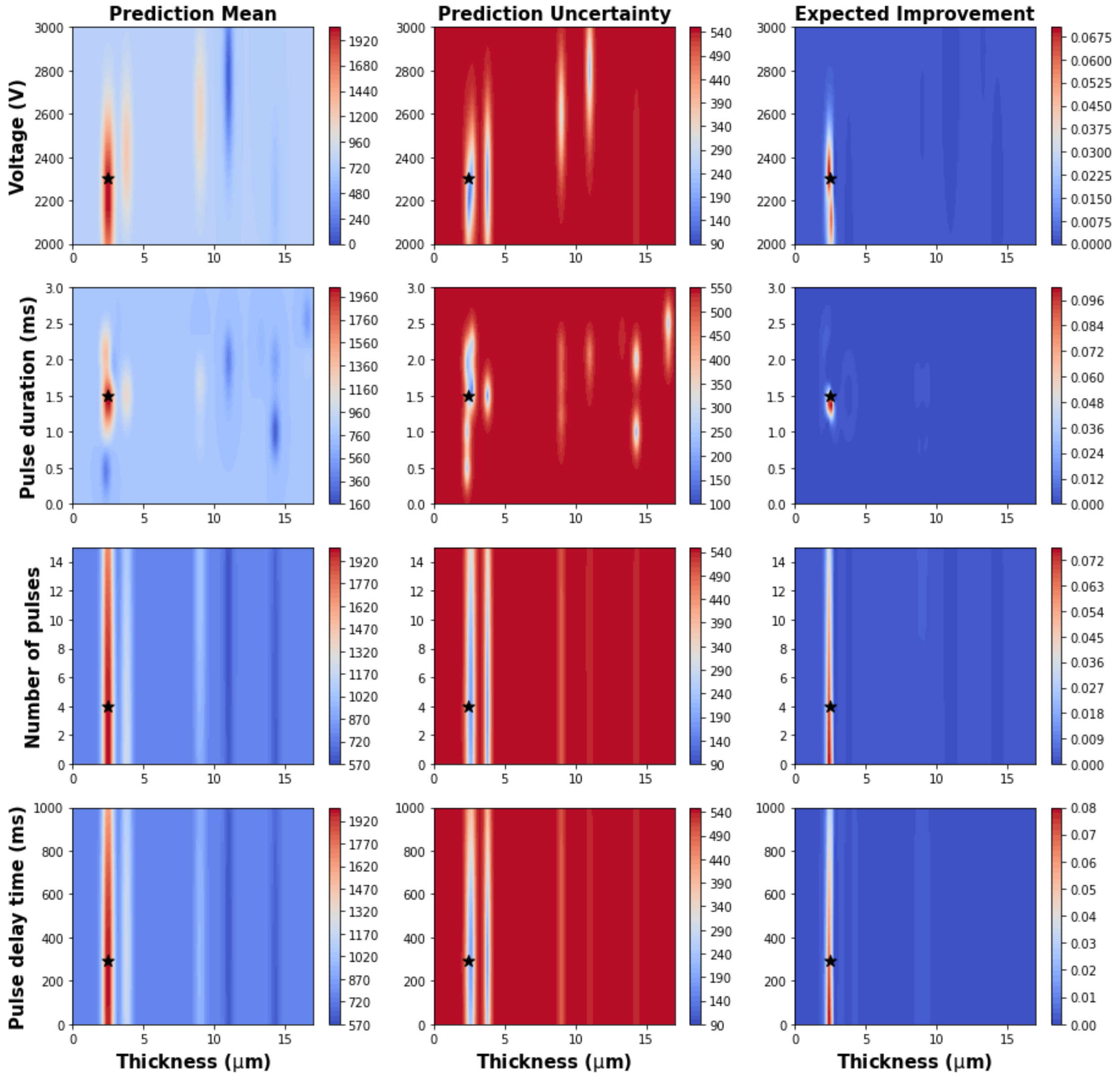

Figure S13. Bayesian optimization prediction mean, uncertainty, and expected improvement from all data except the highest power factor.

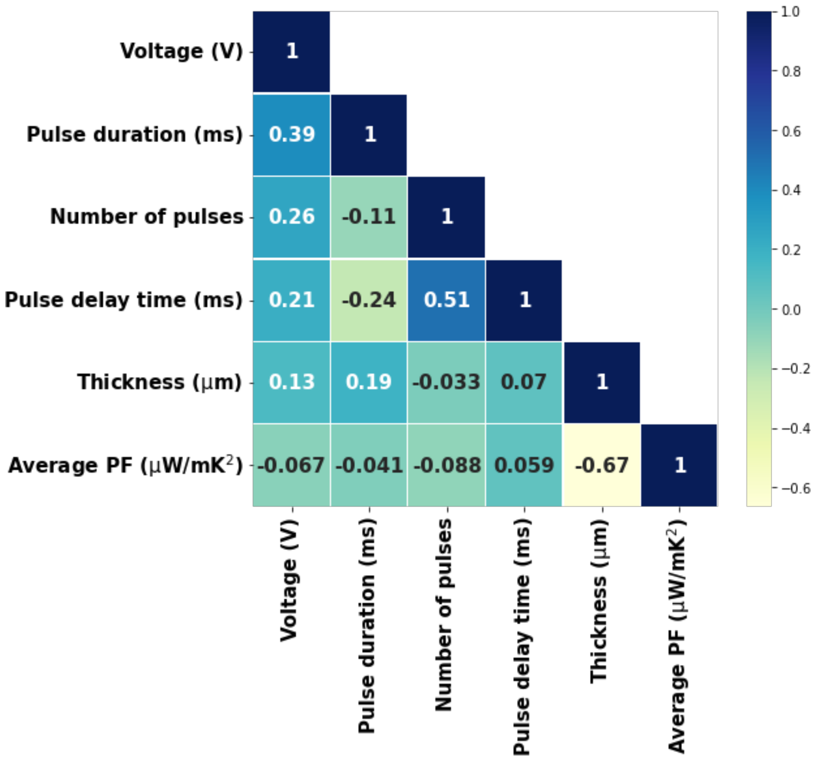

Figure S14. Feature-feature correlation matrix of the top features.

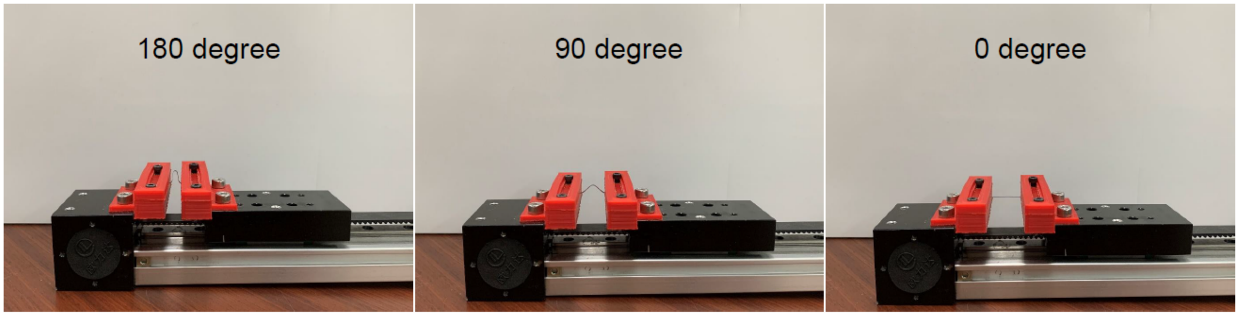

Figure S15. Flexibility test of the flash sintered films under different bending angels.

Table S5. Comparison for flexibility of silver-selenide films with different compositions fabricated using vacuum-assisted filtration technique.

Composition	Bending cycles	Bending radius (mm)	Retained electrical conductivity (%)	Retained PF (%)	Ref.
$Cu_1Ag_4Se_3$	1000	4	93	90	1
PVP-Ag_2Se	1000	4	98	94.5	2
Ag_2Se	1000	4	95.8	90.7	3
$Ag_{1.8}Se$	1000	4	93.3	NA	4
Ag_2Se/Se/polypyrrole	1000	4	93.5	NA	5
β-Ag_2Se	1000	4	93	NA	6
$Ag_{1.96}Se$	1000	5	92.2	92	**This work**

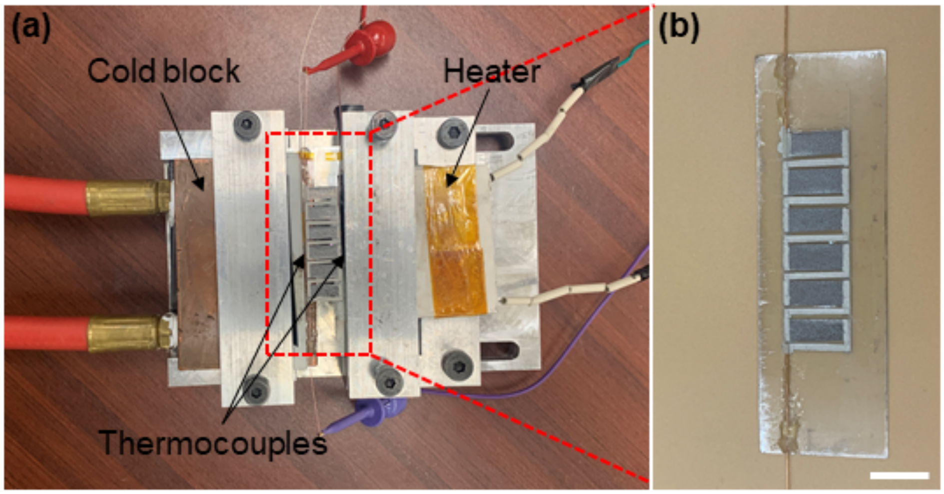

Figure S16. (a) Experimental setup for TEG performance measurement. **(b)** In-plane TEG assembled with six silver-selenide TE films on mica. Scale bar is 1 cm.

Thermal conductivity measurement using Angstrom method

In this work, the Angstrom method,[7] was used to measure the in-plane thermal diffusivity of the unsintered and sintered silver-selenide films under the optimized condition. This measurement was conducted in vacuum (~2 mTorr) and involved applying a periodic heat signal at one end of the film using a function generator (RIGOL DG4062) and the detection of the amplitude and phase of the resultant temperatures at two different locations along the sample using a data acquisition (Keysight 34970A). Two k-type thermocouples (Omega, 5TC 40 AWG), one located near the heater (near-side) and the other located further away (far-side), were used to record the temperature. The frequency range was chosen such that the thermal penetration depth is as large as possible (to ensure a large and detectable temperature oscillation on the far end of the sample) but shorter than the distance between the two thermocouples. Thermal diffusivity (α) was obtained from the following relationship where L is the distance between two thermocouples, dt, and A_1, and A_2 are temperature phase difference, and amplitudes at near-side, and far-side locations, respectively.

$$\alpha = \frac{L^2}{2dt\, ln\frac{A_1}{A_2}}$$

Thermal conductivity (κ) was determined by the measured thermal diffusivity α, specific heat capacity c_p, and density ρ, using the relationship $\kappa = \alpha\rho c_p$ where α, c_p and ρ are thermal diffusivity, specific heat and density, respectively. Schematic illustration of the thermal diffusivity measurement setup using Angstrom method, and phase difference and temperature amplitude variation for near-side and far-side thermocouples are shown in Figure S17.

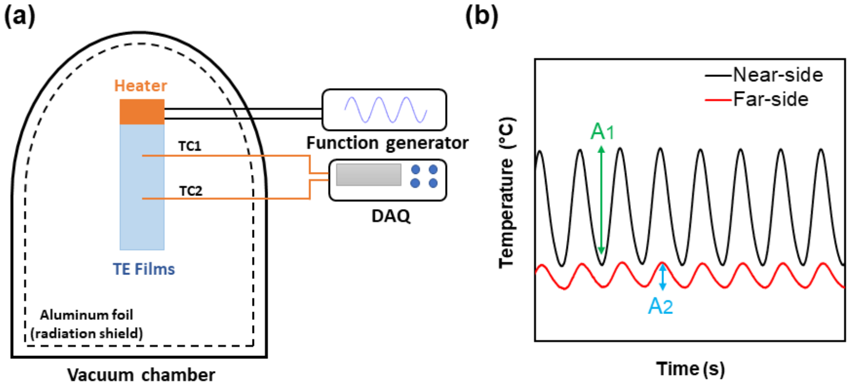

Figure S17. (a) Schematic illustration of the thermal diffusivity measurement setup, and **(b)** recorded temperatures.

To obtain the thermal diffusivity of the silver-selenide films, the thermal diffusivity of the porous filtration membrane is measured initially, and then the combined membrane and silver-selenide film is measured. Modified effective medium theory,[8] was used to extract the thermal conductivity of the silver-selenide film using the following relationship:

$$\alpha_{measured}\left(\rho_{film}c_{film}\frac{A_{film}}{A_{sub}}+\rho_{sub}c_{sub}\right)=\kappa_{film}\frac{A_{film}}{A_{sub}}+\kappa_{sub}$$

where $\alpha_{measured}$ is the combined thermal diffusivity of substrate (porous membrane) and silver-selenide film, and ρ_{film}, c_{film}, A_{film}, κ_{film} are density, specific heat, area, and thermal conductivity of silver-selenide film, respectively. Similarly, ρ_{sub}, $c_{sub,}$ A_{sub}, and κ_{sub} are density, specific heat, area, and thermal conductivity of the substrate. In addition, sample and the vacuum chamber were covered with an aluminum foil to minimize the heat loss through radiation. Moreover, the accuracy of the measurement using Angstrom method was validated by measuring the thermal diffusivity of pure high-density polyethylene and fused quartz with known α. The measurement results agree within 5% of reported values in literature. Despite the challenging nature of thermal conductivity measurement of thin films, the Angstrom method is a well-established technique that has been implemented for thermal conductivity measurement of various materials, including thermoelectric films, polymeric nanocomposites and graphene sheets.[9-12]

Seebeck coefficient measurements

The Seebeck coefficient was measured using a custom-built setup. For Seebeck coefficient measurement, one end of the film is placed on a heater and the other end on a heat sink. Temperature gradient ΔT is measured using two identical k-type thermocouples (Omega, 5TC 40 AWG) with very fine gauge size in order to minimize the cold finger effect. Seebeck coefficient measurement begins by slowly increasing the temperature gradient ΔT while recording ΔT and voltage difference ΔV across the negative leads of the thermocouples (TCs) using a data acquisition (Keysight 34970A). The negative of the slope of the best fit line through the ΔV/ΔT data gives the Seebeck coefficient relative to the Seebeck coefficient the negative lead of the thermocouple. The absolute Seebeck coefficient of the sample is obtained by correcting the measured Seebeck coefficient and accounting for the Seebeck coefficient of the negative lead of the thermocouple wire. For Seebeck coefficient measurement, the instrument was calibrated using a standard constantan sample of known properties.

References

1 Y. Lu, Y. Qiu, K. Cai, Y. Ding, M. Wang, C. Jiang, Q. Yao, C. Huang, L. Chen and J. He, *Energy & Environmental Science*, 2020, **13**, 1240–1249.

2 C. Jiang, P. Wei, Y. Ding, K. Cai, L. Tong, Q. Gao, Y. Lu, W. Zhao and S. Chen, *Nano Energy*, 2021, **80**, 105488.

3 C. Jiang, Y. Ding, K. Cai, L. Tong, Y. Lu, W. Zhao and P. Wei, *ACS Applied Materials & Interfaces*, 2020, **12**, 9646–9655.

4 Q. Gao, W. Wang, Y. Lu, K. Cai, Y. Li, Z. Wang, M. Wu, C. Huang and J. He, *ACS Applied Materials & Interfaces*, 2021, **13**, 14327–14333.

5 Y. Li, Q. Lou, J. Yang, K. Cai, Y. Liu, Y. Lu, Y. Qiu, Y. Lu, Z. Wang, M. Wu, J. He and S. Shen, *Advanced Functional Materials*, 2021, **32**, 2106902

6 Y. Ding, Y. Qiu, K. Cai, Q. Yao, S. Chen, L. Chen and J. He, *Nature Communications*, 2019, **10**.

7 P. G. Kosky, D. H. Maylotte and J. P. Gallo, *International Communications in Heat and Mass Transfer*, 1999, **26**, 1051–1059.

8 M. Ruoho, K. Valset, T. Finstad and I. Tittonen, *Nanotechnology*, 2015, **26**, 195706.

9 T. Varghese, C. Dun, N. Kempf, M. Saeidi-Javash, C. Karthik, J. Richardson, C. Hollar, D. Estrada and Y. Zhang, *Advanced Functional Materials*, 2019, **30**, 1905796.

10 S. Shin, R. Kumar, J. W. Roh, D.-S. Ko, H.-S. Kim, S. I. Kim, L. Yin, S. M. Schlossberg, S. Cui, J.-M. You, S. Kwon, J. Zheng, J. Wang and R. Chen, *Scientific Reports*, 2017, **7**.

11 P. Banerjee, J. Huang, R. B. Ambade, E. Jang, M. Saeidi-Javash, Y. Zhang and D. Madan, *Nano Energy*, 2021, **89**, 106482.

12 M. Saeidijavash, J. Garg, B. Grady, B. Smith, Z. Li, R. J. Young, F. Tarannum and N. Bel Bekri, *Nanoscale*, 2017, **9**, 12867–12873.